LASER & PHOTONICS REVIEWS
www.lpr-journal.org

Direct 3D Imaging through Spatial Coherence of Light

Gianlorenzo Massaro, Barbara Barile, Giuliano Scarcelli, Francesco V. Pepe, Grazia Paola Nicchia, and Milena D'Angelo*

Wide-field imaging is widely adopted due to its fast acquisition, cost-effectiveness, and ease of use. Its extension to direct volumetric applications, however, is burdened by the trade-off between resolution and depth of field (DOF), dictated by the numerical aperture of the system. It is demonstrated that such trade-off is not intrinsic to wide-field imaging, but stems from the spatial incoherence of light: images obtained through spatially coherent illumination are shown to have resolution and DOF independent of the numerical aperture. This fundamental discovery enables to demonstrate an optimal combination of coherent resolution-DOF enhancement and incoherent tomographic sectioning for scanning-free, wide-field 3D microscopy on a multicolor histological section.

1. Introduction

Wide-field imaging is among the most common imaging modalities for the observation and characterization of absorbing specimens, as done, for instance, in bright-field microscopy.[1] Some of the reasons behind its widespread use across many diverse applications are its ease of use, cost-effectiveness, fast acquisition, and its "direct" imaging capability (namely, the availability of the output image in real time, with no need for inverse computation techniques on the collected intensity). Although conventional devices work extremely well with 2D samples, having negligible thickness along the optical axis (z), their use with 3D samples is significantly complicated by the well-known dependence of both resolution and depth of field (DOF) on the numerical aperture (NA) of the imaging device: this dependence results in a strong trade-off between image resolution and DOF, and imposes the need to z-scan the whole sample in order to collect the complete volumetric profile. The operation of z-scanning requires that either the imaging device or the sample itself are mechanically shifted along the optical axis, so as to change the plane in focus and perform multiple acquisitions of different transverse planes.[2,3] The intrinsically long acquisition required by moving components implies limited in vivo applicability and comes with further disadvantages, such as the need for precise stabilization, requiring large and heavy devices, costly mechanical parts with the required precision, as well as high maintenance costs, which preclude the use of scanning microscopes in low-budget applications. The limitations of axial scanning become particularly relevant in large-NA devices, where the higher resolution comes at the expense of a narrower DOF. This has detrimental effects on the number of axial measurements necessary to characterize the entire sample, so that a common option to keep the measurement time low is to under-sample along the optical axis, with a consequent loss of information. In 3D imaging, resolution, axial sampling, and acquisition speed are thus in direct conflict. Several approaches have been proposed in the literature to address this problem, optical coherence tomography (OCT) being one of the most noticeable examples.[4] However, in all cases, the limitations imposed by the NA of the imaging system persist. In OCT, for example, small NA are required, at the expenses of resolution and signal-to-noise ratio (SNR), for addressing the loss of intensity implied by large-NA optics[5]; dedicated approaches have been developed to address this issue, at the expense of the reconstruction speed.[6,7] A recent and rapidly developing approach to scanning-free wide-field 3D microscopy is light-field (LF) imaging, where direct images of thick samples containing heavily defocused planes are acquired and then "refocused," in post-processing.[8–12] Directional information about light from the sample is in fact acquired by a microlens array and

G. Massaro, F. V. Pepe, M. D'Angelo
Dipartimento Interateneo di Fisica
Università degli Studi di Bari Aldo Moro
Bari 70125, Italy
E-mail: gianlorenzo.massaro@uniba.it
G. Massaro, F. V. Pepe, M. D'Angelo
Istituto Nazionale di Fisica Nucleare (INFN), Sezione di Bari
Bari 70125, Italy
B. Barile, G. P. Nicchia
Dipartimento di Bioscienze, Biotecnologie e Ambiente
Università degli Studi di Bari Aldo Moro
Bari 70125, Italy
G. Scarcelli
Fischell Department of Bioengineering
University of Maryland
College Park, MD 20742, USA
G. P. Nicchia
Institute for Organic Synthesis and Photoreactivity
National Research Council of Italy
Bologna 40129, Italy
G. P. Nicchia
Dominik P. Purpura Department of Neuroscience
Albert Einstein College of Medicine
New York, NY 10461, USA

The ORCID identification number(s) for the author(s) of this article can be found under https://doi.org/10.1002/lpor.202301155

DOI: 10.1002/lpor.202301155

employed, in post-processing, to perform software z-scans with similar features to the typical mechanical scans. LF devices thus enable scanning-free single-shot acquisition of a 3D sample, but its fast acquisition comes at the expenses of a dramatic loss of resolution, well beyond the diffraction limit.[13] In fact, due to its geometric-optics-based working principle, the maximum achievable DOF is defined by the circle of confusion (CoC), namely, by the projection of the lens aperture over the acquired defocused planes.[14] The resolution of the refocused images is thus not determined by the Airy disk, as is typically the case in microscopy, but is rather dominated by the geometrical effects of defocusing, as typically occurring in photography. In addition, the lenslets introduce an even stronger trade-off between resolution and DOF, consisting in the loss of resolution at focus with the improvement of the axial performance.[15]

In this work, we show that the "transverse spatial coherence" of light illuminating a given sample can be exploited in direct wide-field imaging to obtain a breakthrough improvement of the image resolution over large DOF. In fact, our work brings in, and exploits, the fundamental discoveries that resolution and DOF of coherent images are NA-independent and are related by a square-root law, as opposed to the typical linear dependence defining the CoC of incoherent imaging. In this respect, it is worth noticing that while the peculiarities of focused images, whether coherent or incoherent, are well known,[16,17] the properties of coherent defocused images have been so far mostly unexplored, with the only exception of the very special case of collimated light illumination.[17–19] Our work fills in this gap and exploits the result for addressing an open challenge of direct wide-field imaging.

The results are articulated as follows. At first, the properties of coherent imaging of out-of-focus objects are theoretically investigated and experimentally validated. In such a context, we find that neither the NA nor the design of the imaging system affects the quality of defocused coherent images; the NA-dependent trade-off between resolution and DOF defined, in incoherent defocused images, by the CoC is found to naturally disappear when illuminating the sample with spatially coherent light. This discovery is supported by the introduction of a dedicated formalism, providing an unbiased image quantifier named "image fidelity," which enables to study the properties of coherent images and to fairly compare them with the ones of conventional incoherent imaging. In the second part of the paper, we profit from the aforementioned properties to design a direct, scanning-free, wide-field 3D microscope, which allows for the typical tomographic reconstruction of multicolor LF imaging, but optimally combined with enhanced resolution, both at focus (where we recover Rayleigh-limited resolution) and in the surrounding volume. After discussing the working principle and the expected properties of a direct coherent wide-field volumetric miscroscope, we experimentally demonstrate its imaging capability on a histological sample, and show 3D reconstruction compatible with absorbing non-fluorescent dyes routinely used for histochemistry.[20]

Unlike typical bright-field microscopes, where the sample is illuminated by spatially incoherent light emitted by an extended source,[1,21] the proposed 3D microscope exploits a dedicated coherent illumination strategy, where LEDs in a 2D array are sequentially activated and spatial coherence is acquired through propagation.[22] To better appreciate the novelty and breakthrough of the proposed and developed microscope, it is worth recalling that spatial coherence is typically used in "indirect" imaging modalities relying on time-consuming post-processing algorithms aimed at recovering phase information about the sample. Typical examples are holography[23,24] and ptychography,[25] which achieve super-resolution, wavefront reconstruction, and correction of optical aberrations at the expense of imaging reconstruction time. 3D amplitude and phase reconstruction[19,26,27] has recently been achieved within a microscope based on both sequential multi-angle plane-wave illumination from LED arrays and recursive phase-retrieval algorithms. However, all such coherent imaging techniques are indirect, due to the required time-consuming algorithms and are thus not suitable for real-time imaging.[28,29] On the contrary, no phase retrieval and time-consuming post processing of the acquired images are required in our approach, paving the way toward 3D real-time imaging.

2. Experimental Section

Throughout the whole paper, we shall refer to coherent imaging whenever the coherence area of the illumination,[30] on the sample, is larger than the spatial features of the sample one wishes to resolve.[22] According to the size of the details composing a given object, an imaging system might thus behave coherently for object details smaller than the coherence area, and incoherently for larger details. We shall analyze the transition from one regime to the other, namely, which experimental conditions must be satisfied for a system to pass from an incoherent to a coherent behavior, later on in Sections 3 and 4. For the sake of simplicity, we shall now disregard the effects of partial coherence and only focus on the limiting cases.

2.1. Resolution and DOF in Coherent Imaging

We shall start by focusing on the different imaging performance of coherent and incoherent imaging, from both a qualitative and a quantitative viewpoint. In panels (a) and (b) of **Figure 1**, obtained through simulations, we report two typical examples of incoherent and coherent imaging, respectively, as obtained by changing the illumination with the same imaging system. Incoherent illumination is achieved, as reported in the upper part of panel (a), by placing an extended spatially incoherent source at a small enough distance from the sample, so that coherence acquired by propagation can be neglected. The upper part of panel (b) suggests one of many possible ways for obtaining coherent illumination from an incoherent source: since the coherence area on the sample scales proportionally with the ratio between the source distance and the source diameter, coherence is obtained by reducing the source size.[31] An obvious alternative would be to employ laser light illumination, but the presented results are not limited to this scenario. In the lower part of panels (a) and (b), we report the corresponding incoherent and coherent images of a 2D double-slit mask, both focused (left panels) and defocused (center and right panels). Defocused images have very distinctive features depending on the spatial incoherence or coherence of light on the sample: while incoherent images tend to quickly blur upon defocusing, coherent images do not blur. This is even more apparent in panel (c), reporting a section, in the (x, z) plane, of the 3D

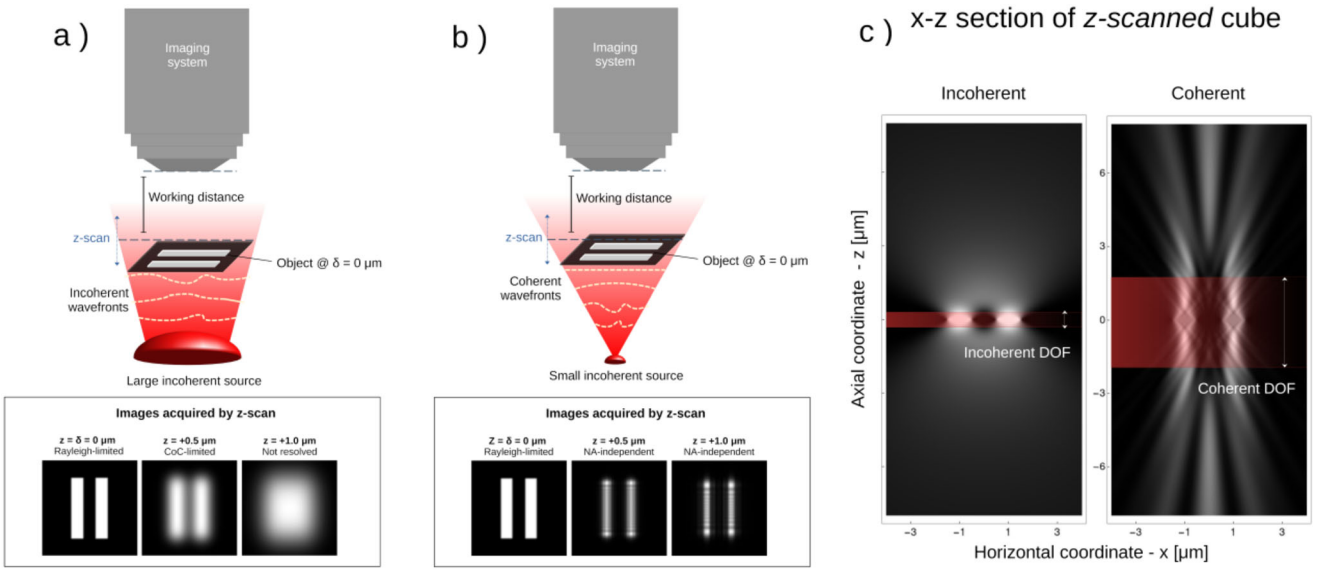

Figure 1. Simulation of the resolution and DOF enhancement enabled by coherent imaging, as compared to incoherent imaging. a) Incoherent imaging setup (top) and corresponding focused and defocused images (bottom). In the setup, a transmissive sample (a double-slit mask) is illuminated by the incoherent wavefronts coming from an extended source and is imaged by a conventional imaging system. The focused image (bottom left) is obtained by placing the sample at the working distance of the imaging system; the defocused images (bottom center and right) are obtained by z-scanning of the sample. b) Coherent imaging setup (top) and corresponding focused and defocused images (bottom). In the setup, the same transmissive sample as in panel (a) is illuminated by spatially coherent light from a small incoherent source, and is imaged by the same imaging system. The focused (bottom left) and defocused (bottom center and right) coherent images are obtained by placing the sample at exactly the same positions as in panel (a). c) Axial section of the 3D cube obtained by z-scanning the sample in the setups of panels (a) and (b), namely, in the case of incoherent (left panel) and coherent (right panel) illumination.

cubes obtained by mechanically z-scanning the two-slit mask, in both cases of incoherent (left panel) and coherent (right panel) imaging. In incoherent imaging, z-scanning quickly results into a flat intensity distribution as the object is moved out of focus; in coherent imaging, on the contrary, the intensity distribution contains rich spatial modulation and object details stay well separated from each other over a much longer axial range compared to the corresponding incoherent images. Transmissive details of the sample are thus "resolved" at a much larger distance from the plane in focus, before being completely altered by "diffraction". Coherent imaging thus appears to have much longer DOF (or, equivalently, higher resolution of defocused images) than incoherent imaging, and image degradation is not due to blurring.

Let us now move to a quantitative description of the observed phenomena. The differences between coherent and incoherent systems can be traced back to the different underlying image formation processes, as formally expressed by the intensity distributions[17]

$$I_{\mathrm{inc}}(\boldsymbol{r}) = \left|\mathcal{A}(\boldsymbol{r})\right|^2 * \left|\mathcal{P}(\boldsymbol{r})\right|^2, \quad I_{\mathrm{coh}}(\boldsymbol{r}) = \left|\mathcal{A}(\boldsymbol{r}) * \mathcal{P}(\boldsymbol{r})\right|^2 \tag{1}$$

where $\mathcal{A}(\boldsymbol{r})$ is the complex transmission function of the object, $\mathcal{P}(\boldsymbol{r})$ is the Green's function describing the field propagation through the optical system, and $f * g$ denotes the convolution between two complex-valued functions, f and g. Unlike the incoherent image formation process, which is linear in the "optical intensity," coherent imaging is non-linear with respect to the object $\mathcal{A}(\boldsymbol{r})$. Therefore, although the same quantities are involved in both intensity distributions of Equation (1), those contributing to the incoherent image formation are real and positive, whereas coherent imaging is sensitive to both the amplitude and phase of complex functions describing both the field distribution within the sample and its propagation through the imaging system.[19,24–26]

Upon neglecting optical aberrations, the "coherent" (i.e., complex) PSF $\mathcal{P}(\boldsymbol{r})$ of Equation (1) can be decomposed into two contributions:

$$\mathcal{P}(\boldsymbol{r}) = \mathcal{D}_{z-\delta}(\boldsymbol{r}) * \mathcal{P}_0(\boldsymbol{r}) \tag{2}$$

where $\mathcal{P}_0$ is the complex PSF describing the focused coherent image and determining the well-known Airy disk,[32] and $\mathcal{D}_{z-\delta}$ represents the field propagation over a distance $z-\delta$, with δ and z the axial coordinates of the object point and of the plane in focus, respectively. Depending on the placement of the sample and the numerical aperture of the device, the quality of the output image can thus be dominated either by the effects of out-of-focus propagation or by the Airy disk, with the two effects blending into each other only when the object is placed close to (but not perfectly on) focus.

The corresponding transition between the focused and defocused image is well known in incoherent imaging: at focus, both the resolution (λ/NA) and the DOF (λ/NA^2) are determined by wave optics (Airy disk), with λ the illumination wavelength. However, as the object is moved outside of the natural DOF of the focused device, the PSF $\mathcal{P}$ is dominated by geometrical optics effects and reduces to the circle of confusion (namely, the projection of the lens aperture onto the defocused image plane).[14] This

induces a typically circular blurring with a radius proportional to both the defocusing $|z-\delta|$ and the effective lens radius.

2.2. Image Fidelity

The different physics regulating coherent and incoherent imaging helps developing an intuition about the different behavior observed in Figure 1, but does not suffice to quantitatively compare the resolution and DOF of coherent and incoherent imaging. In fact, image quality estimators typically used for characterizing imaging performance, from two-point resolution criteria, such as Rayleigh's and Abbe's,[16,33] to more advanced ones, such as modulation transfer functions,[34] all rely on the linearity of the (incoherent) image formation and the positiveness of the PSF, and thus fail in assessing the performance of a nonlinear process such as coherent imaging. To quantify and compare the performance of coherent and incoherent imaging systems, we thus introduce a general-purpose quality estimator: the functional F_A, which we shall refer to as "image fidelity," defined as a positive quantity $F_A[I(\boldsymbol{r})]$ that directly compares the intensity distribution $I(\boldsymbol{r})$ of the image with the original intensity profile of the object $A=|\mathcal{A}|^2$, namely,

$$F_A[I]=\int \sqrt{A\left(\frac{\boldsymbol{r}}{M}\right)I(\boldsymbol{r})}\,d\boldsymbol{r} \tag{3}$$

where M is the magnification of the imaging system in its plane in focus. Both A and I are normalized quantities for the definition of the fidelity to be consistent and to saturate to unity in the ideal case of perfect imaging ($I=A$). Being completely independent of any detail of the image formation process, the fidelity enables performing image quality evaluation through any imaging device, as long as the shape of the known reference object is known: resolution and DOF shall thus be defined as the minimum object size and the maximum axial range producing a "faithful" image, as identified by a threshold set to the fidelity. Both these definitions apply equally well to focused and defocused images, thus enabling to study how resolution changes with defocusing. In view of a direct comparison with incoherent imaging, sensitive only to the "intensity" transmitted by the sample, our study will now be restricted to object that are non-diffusive and carry no phase information (namely, $\mathcal{A}=|\mathcal{A}|\geq 0$ uniformly in the sample).

2.3. Experimental Setup

In the "Results" section, theory is experimentally validated in a microscopy-oriented optical setup. The employed optical microscope consists of a standard combination of an objective lens (Nikon Plan Apo λ20×, NA = 0.75) and a tube lens (Thorlabs TTL200). The camera (sCMOS, Andor Zyla 4.2) is placed in the second focal plane of the tube lens, so that, at focus, the plane at the working distance from the objective is imaged with magnification 20×.

Illumination is provided by an array of LEDs, which serves both as source of light with tunable coherence, and as a source of quasi-point-like emitters at known transverse position. As we shall discuss, this is required for 3D reconstruction. We used a 22×22 array of 2427 WS2812B RGB mini LEDs. In order to obtain a large coherence area when a single LED is lit, the array has been placed at a distance $L=110$mm from the working distance of the microscope. In this configuration, incoherent illumination is easily obtained by illuminating the sample with all the LEDs simultaneously lit. To speed up acquisition, we have worked with a 16×16 subset of LEDs. The array of WS2812B was piloted by an external microcontroller (Arduino UNO). Since the employed camera is monochrome, the reported multicolor measurements are obtained by performing three subsequent measurements, one per color channel, and the results are then combined into a single RGB image.

The multicolor 3D imaging capabilities of the technique we propose are demonstrated on a histological section of mouse brain. The tissues were isolated from 8 months old C57BL/6 mice and fixed in 4% PFA solution overnight (O/N) at 4°C. Fixed brains were then washed for 1 h in PBS, soaked in increasing concentrations of PBS-sucrose solutions (5%, 10%, 20%, O/N 30%), embedded in Tissue-Tek O.C.T. compound (Sakura, The Netherlands), and frozen at −80° C. Ten micrometer thick sagittal slices were obtained using a cryostat (CM 1900; Leica, Wetzlar, Germany) at −20° C. Rehydrated sections were stained using the hematoxylin/eosin method to label nuclei (Mayer's hematoxylin, Sigma) and cytoplasm (eosin, Carlo Erba), dehydrated in graded ethanol, and cleared with xylene solution (PanReach Applichem, Darmstadt, Germany). Glass coverslips (0.15 mm thick) were then mounted onto stained sections using Canada Balsam (Millipore, Burlington, Massachusetts, USA).

Procedures involving animals were carried out in compliance with the European and Italian directives on animal use for research and the approval of the Italian Health Department (Approved Project no. 92 n°710/2017-PR). The experiments were designed to minimize the number of animals used and animal suffering.

3. Results

3.1. Resolution Limits of Coherent Imaging

The plot reported in **Figure 2** employs the "fidelity" to offer a quantitative interpretation of the coherent and incoherent z-scans reported in Figure 1c. The colored areas in Figure 2 highlight how far from the plane in focus (abscissas) an s-sized object (ordinates) can be placed to produce an image with fidelity higher than 95%. The orange area refers to spatially incoherent illumination, whereas the blue area refers to the coherent case.

As we shall derive shortly, the dashed curves delimiting the high-fidelity regions associated with coherent and incoherent imaging result from two different physical regimes. Such curves offer a clear perspective on the physical mechanisms regulating the two image formation processes and enable quantifying the resolution versus DOF trade-off in the two cases. Hence, such boundaries can be interpreted as "resolution limit curves," giving the functional dependence of the resolution on the displacement from focus, at the threshold value of the image fidelity, above which an image is considered to be resolved. For any object shape, the resolution curves are obtained from the expression of the image fidelity, written in terms of image parameters.

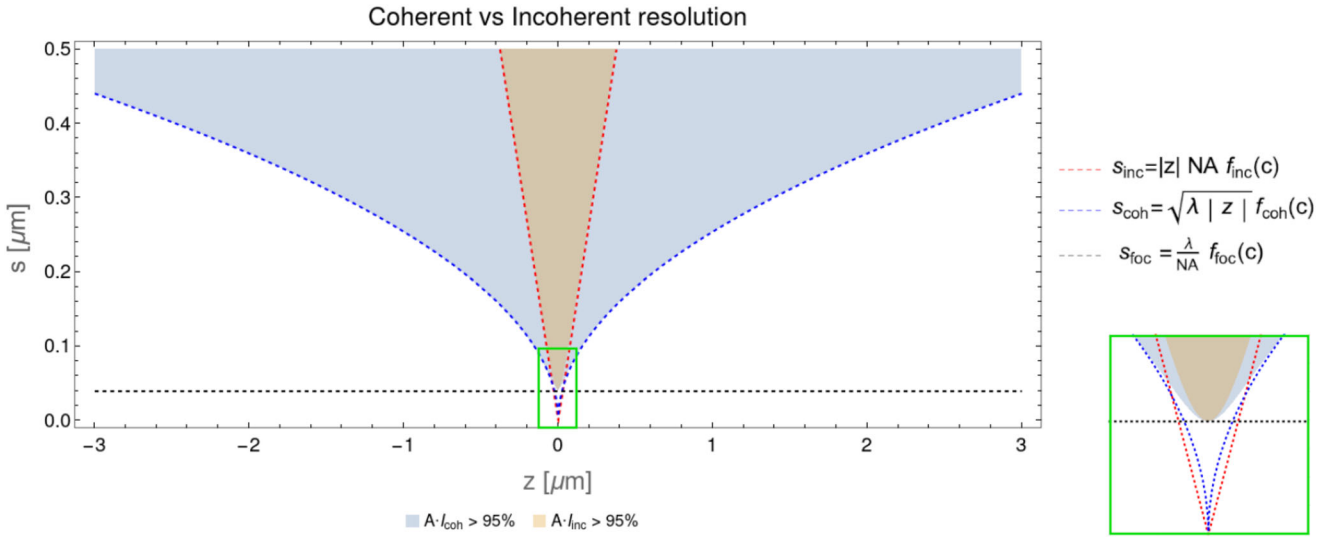

Figure 2. Theoretical image fidelity in coherent and incoherent imaging. The colored areas (blue for coherent illumination, orange for incoherent illumination) highlight the regions in which an s-sized object placed at an axial coordinate z can be imaged with a fidelity larger than 95%, with $z = 0$ identifying the position of the object in focus. The black dashed line is the fidelity equivalent of the Rayleigh criterion, intended as the minimum object size that can be imaged faithfully. The orange dashed curve is the NA-dependent geometrical circle of confusion at 95% fidelity, obtained by evaluating the fidelity in the geometrical optics approximation. The blue dashed line represents the curve of 95% fidelity obtained in the wave optics regime (namely, by considering the free space coherent propagation of the field) in the case of infinite NA of the imaging system. The imaging system is a 20× microscope with NA = 0.5, illuminated with monochromatic light with wavelength 500nm. The object is a mask with a single transmissive detail with Gaussian shape of width s.

In our case, the parameters are: the dimension s of the features of the sample, the axial coordinate δ where the sample is located, and the axial location z of the plane focused by the imaging system. The image fidelity associated with $I(\boldsymbol{r}) = I(\boldsymbol{r}; \delta - z, s)$ is thus a two-variable function: $F_A[I](\delta - z, s)$. Since the quality of the image, upon mechanical z-scanning, only depends on the relative distance between the object and the focused plane, we shall set for simplicity $\delta = 0$ and interpret z as the relative "defocusing" distance. In order to deal with analytical results, Figure 2 reports the fidelity plots obtained with a Gaussian transmissive slit as the object, as well as a Gaussian PSF; the imaging system is a 20× magnification microscope with NA = 0.5. All the analytical expressions are reported in the Supporting Information. By studying the analytical expression of $F_A[I](z, s)$, exact expressions of relevant image quantifiers can be extracted. For instance, $F_A[I](0, s)$ gives the image fidelity in the plane in focus, as a function of the object size. If the fidelity threshold is set to c, the Rayleigh-limited resolution is obtained by inversion of the equation $F_A[I](0, s_{\text{foc}}) = c$. Both for coherent and incoherent imaging, one obtains

$$s_{\text{foc}} = \frac{\lambda}{\text{NA}} f_{\text{foc}}(c) \tag{4}$$

where $f_{\text{foc}}(c)$ is a coefficient depending of the threshold image fidelity, amounting to 0.157 for $c = 0.95$ (as chosen in Figure 2). Apart from the multiplying constant, which only depends on the arbitrary choice of the threshold on the fidelity, the equation corresponds to the well-known diffraction-limited resolution of focused imaging systems (dashed black line in Figure 2), as determined by the Airy disk. The analysis in terms of fidelity thus recovers the well-known fact that the optical performance of focused coherent and incoherent systems is the same.

The differences between the resolution and DOF of coherent and incoherent imaging emerge when analyzing "defocused" images in two different physical regimes. The geometrical optics regime is knowingly explored by considering the fidelity in the limit $\lambda \to 0$, namely,

$$F_{\text{geom}}[I](z, s) = \lim_{\lambda \to 0} F_A[I] \tag{5}$$

If this physical regime is investigated in the incoherent imaging case, the implicit curves $F_{\text{geom}}[I_{\text{inc}}] = c$, in the (z, s) plane, have an explicit expression, which, unsurprisingly, prescribes the well-known circle of confusion of geometrical optics:

$$s_{\text{geom}}(z) = \text{NA}\,|z|\, f_{\text{geom}}(c) \tag{6}$$

with $f_{\text{geom}}(0.95) = 1.97$. As shown in Figure 2, the trend defined by the CoC (dashed orange line) perfectly traces the boundary of the fidelity area associated with incoherent imaging. Hence, the fidelity analysis confirms that wave optics has negligible effects on the optical performance of an incoherent system when the sample is moved away from perfect focus. By exploring the same physical limit in the case of coherent imaging, the obtained analytical expression does not describe any physically relevant situation and does not have a counterpart in the shape of the fidelity region.

In the coherent case, interesting results are obtained by investigating the opposite regime, namely by neglecting geometrical effects. As explained in further detail in the Supporting Information, this is done by considering the radius of the limiting

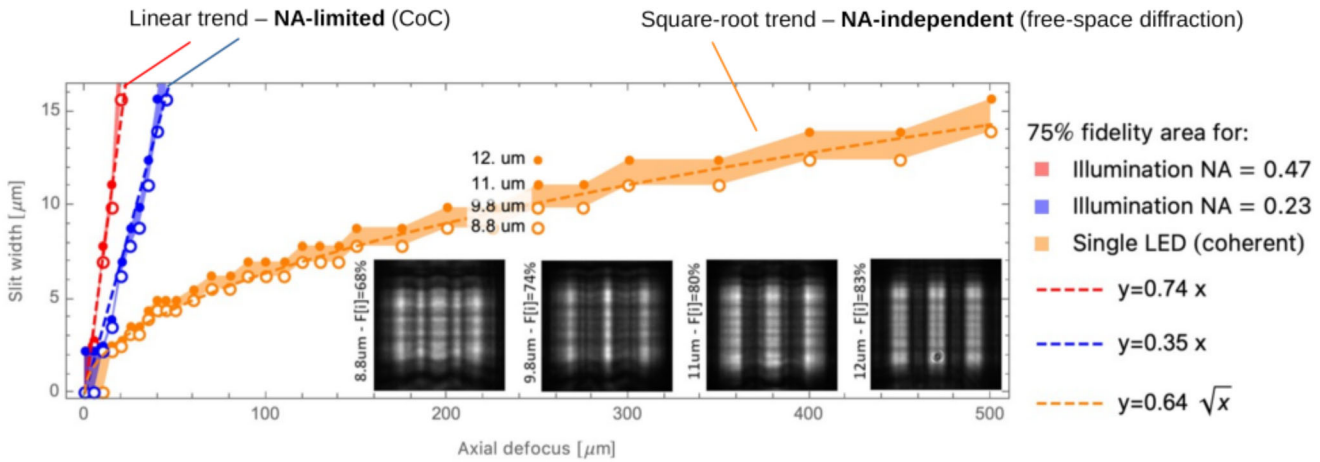

Figure 3. Experimental comparison of resolution and DOF in incoherent and coherent imaging. Comparison of the resolution-DOF trade-off in two cases of incoherent imaging (red and blue points), corresponding to two different illumination NA, and for coherent imaging (orange points). An image is considered to be resolved when the corresponding fidelity is at least 75%: areas of 75% fidelity (colored regions) are identified by the smallest slit width $F[I] < 75\%$ (empty circles) and the largest slit width imaged with $F[I] > 75\%$ (full circles). The sample is a triple-slit USAF test target. The four images reported in the panels as a reference quality of the targeted fidelity are taken at the same axial distance of $z = 250\,\mu$m and correspond to the four different values of the slit width.

aperture $l \to \infty$, so as to completely ignore the influence of the imaging device. This condition is equivalent to considering an imaging system where the image formation process is solely governed by diffraction, from the object plane up to the plane in focus; in fact, in Equation (2), $\mathcal{P}(\boldsymbol{r}) \xrightarrow{\text{NA}\to\infty} \mathcal{D}_z(\boldsymbol{r})$, indicating that no CoC exists in this case. Upon setting a threshold c to the fidelity of a coherent system with infinite NA

$$F_{\text{diff}}[I_{\text{coh}}] = \lim_{l\to\infty} F_A[I_{\text{coh}}] \tag{7}$$

we obtain the resolution limit curves

$$s_{\text{diff}}(z) = \sqrt{\lambda|z|}\, f_{\text{diff}}(c) \tag{8}$$

with $f_{\text{diff}}(0.95) = 0.396$. This square-root scaling of the resolution with defocusing perfectly reproduces the boundary of coherent imaging out of the plane in focus, as reported by the blue dashed line in Figure 2. As in the previous case, exploring the same physical limit in the case of incoherent illumination yields no interesting conclusion. The NA-independent square-root scaling of reslution versus DOF is certainly among the most relevant findings of this paper.

In conclusion, the resolution versus DOF trade-off of coherent and incoherent imaging are defined by two entirely different processes: the geometrical CoC (hence, the system NA) is basically the only factor limiting the resolution of defocused incoherent imaging; on the contrary, the aperture size and optical design of the imaging system play no role in coherent imaging, where the sole responsible for image degradation is diffraction and free-space space propagation from the object to the observation plane. The different resolution scaling of coherent and incoherent imaging can also been interpreted in terms of a substantial DOF advantage of the former over the latter. In fact in coherent imaging, the axial range in which the object is resolved scales quadratically with the object size, rather than linearly. This property, as we shall see, can be exploited to achieve coherent 3D imaging with extended axial reconstruction capabilities.

In **Figure 3**, we report the experimental demonstration of the theoretical predictions discussed above. In particular, we show that coherent illumination enables a four times larger DOF at 2 μm resolution and an almost 20 times larger DOF at 10 μm resolution, with respect to incoherent illumination. The experimental images shown in the figure are obtained by illuminating a USAF test target with green light from the LED array. Figure 3 experimentally proves that the resolution of a defocused coherent imaging system (orange), analyzed in terms of fidelity, obeys the expected square-root law. Incoherent imaging, also tested in terms of fidelity, shows the expected NA-dependent linear trend, of Equation (6). In particular, to study the effect of reducing the NA, we have tested the incoherent system with two illumination NA (blue and red), obtained by changing the areas of lit LEDs on the array (red data correspond to 16×16 lit LEDs, resulting in NA = 0.47; blue data to 8×8, resulting in NA = 0.23.). For coherent imaging, the illumination distance and transverse size of the only lit LED was chosen to ensure a large coherence area. For both coherent and incoherent imaging, an image is considered to be resolved when the corresponding fidelity is at least 75%. Therefore, the areas at 75% fidelity in Figure 3 (colored regions) are defined, one the one side by the smallest slit width imaged with fidelity over 75% (empty circles), and on the other side, by the largest slit width imaged with fidelity lower than 75% (full circles). The four triple-slit images reported in the figure are obtained with coherent illumination, with the sample at a displacement of $z = 250\,\mu$m from the plane in focus. For such displacement, all the slit sizes below 8.8 μm resulted in a sub-75% fidelity, whereas all slits above 9.8 μm resulted in over 75% fidelity, indicating that, for a 250 μm displacement, the 75%-threshold curve passes between those two values.

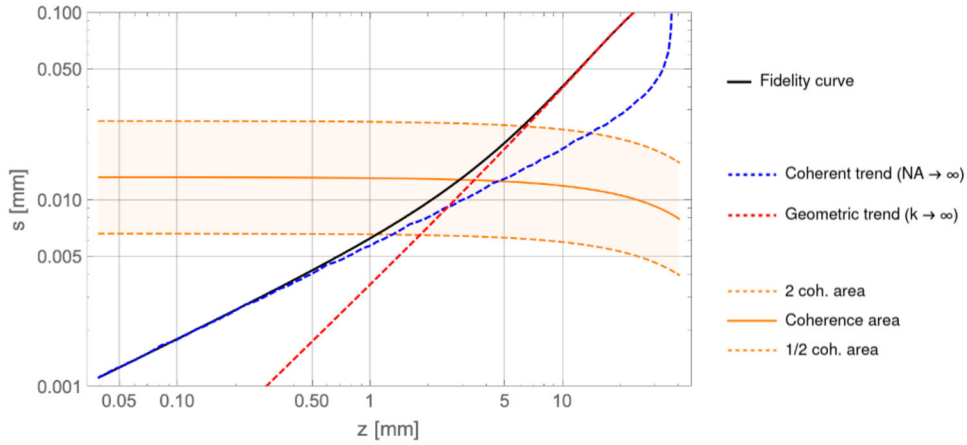

Figure 4. Effect of partial coherence in the transition from coherent to incoherent imaging. Log-log plot of the 95%-fidelity (black continuous line) evaluated in the case of partial coherence due to the finite transverse size of the light source. The dashed red and blue curves are the 95%-fidelities evaluated, respectively, in the geometric optics approximation and in wave optics but with infinte NA. All curves are obtained by considering a microscope with NA=0.5, illuminated by a green light emitter placed at 11 *rmcm* from its plane in focus and having a Gaussian intensity profile of width $w = 0.3$mm; the object is a Gaussian slit of width *s*. The two dashed orange lines identify, for each defocusing *z*, the values of the slit width *s* corresponding to 1/2 (lower curve) to 2 (upper curve) times the coherence area; the orange colored area identify the values of *s* for which partial coherence enters into play giving rise to the transition from incoherent to coherent imaging.

In microscopy and bright-field imaging in general, it is known that collimation implies DOF augmentation.[32] However, the square-root trend we have demonstrated both theoretically and experimentally is the result of an entirely different physical phenomenon that cannot be understood in terms of source collimation, but only in terms of spatial coherence. The conventional (incoherent imaging) explanation of DOF improvement through source collimation, in fact, is related to the divergence of the illuminating beam becoming smaller than the acceptance angle of the optical devices; the optical properties of the imaging device are thus no longer dictated by the NA of imaging device, but rather by the effective NA defined by the illumination itself. This effect is profoundly different from the DOF extension enabled by spatial coherence, where collimation is by no means a requirement. The presented DOF advantage, in fact, expected to be maintained even with a quasi-infinite illumination NA, as one could get by bringing the illumination stage in extreme proximity to the sample and employing smaller sources, such as quantum dots and single-molecule LEDs.

To gain more insight about the role played by the NA of the illumination system, we shall now study the transition from incoherent to coherent imaging and consider the general case of a finite-sized source, matching the experimental conditions of Figure 3. In **Figure 4**, we plot the theoretical 95%-fidelity curve (solid black line) of the image of a transmissive mask (an *s*-sized slit) as a function of its distance from a *w*-sized "incoherent" emitter; strictly speaking, *z* is the distance of the object from the plane in focus, but its variation naturally changes the object-to-source distance as well. When the object is so close to the source that the spatial coherence acquired through propagation towards the sample is smaller than *s*, the resolution versus DOF trade-off is determined by the numerical aperture of the "illumination," as expected in a conventional system; this is demonstrated by the overlap of the evaluated fidelity (black line) with the one obtained in the geometrical optics approximation (red dashed line), for large values of *z*. In this regime, imaging is thus incoherent. However, as the object is moved farther away from the source, the coherence area on the object becomes proportionally larger to the point where coherence effects become dominant, and the fidelity trend (black line) detaches from the geometrical optics prediction and overlaps on the coherent trend (dashed blue line), completely NA-independent. The yellow region highlights the transition from the incoherent to the coherent imaging, and shows that coherent effects enter into play, as predicted, when the coherence area becomes comparable to the details one wishes to resolve. Figure 4 shows that the fidelity curve expected for object details smaller than roughly half of the coherence area is purely coherent, whereas, for an object size double the coherence area, imaging becomes purely incoherent.

3.2. Coherent 3D Imaging with Incoherent Sectioning Capability

The newly discovered properties of direct coherent images can be integrated with the strong axial localization capability of incoherent imaging to achieve scanning-free 3D wide-field imaging of absorbing samples with enhanced volumetric resolution. In fact, spatially coherent illumination will enable a (NA-independent) square-root scaling of transverse resolution, thus offering high lateral resolution over a long DOF; at the same time, the axial sectioning typical of spatially incoherent illumination entails, in the wide DOF accessed through coherence, a precise sectioning capability, as enabled by large-NA tomographic systems.[35] We should clarify that, in this context, the concepts of DOF and axial resolution are rather distinct: while the DOF represents the axial length of the volume where object details of a given size can be faithfully imaged, the axial resolution represents the axial sectioning capabilities, namely, how finely transverse planes within the DOF can be isolated along the axis.

3.2.1. Theory

The underlying principle for achieving high-resolution 3D imaging within a direct wide-field coherent system is similar to LF imaging: in both cases, information about the propagation direction of light enables scanning-free volumetric reconstruction. However, while LF imaging acquires the required directional information by means of the microlens array, our proposal prescribes to do it with spatially coherent illumination of the sample from different locations. Our approach will be shown to come with two major advantages: a much larger DOF, as defined by the square-root (as opposed to linear) scaling of the resolution with defocusing, and Rayleigh-limited images at focus.

In the proposed scheme, 3D information about the sample is acquired by accessing the 4D "light-field" function $I(\boldsymbol{r}_0, \boldsymbol{r})$, where $\boldsymbol{r}_0$ is the transverse coordinate of a point-like emitter enabling spatially coherent illumination of the sample, and $\boldsymbol{r}$ is the transverse coordinate of the collected image. Sampling of the complete 4D function is performed by sequentially sweeping an illumination plane made of point-like emitters centered in $\boldsymbol{r}_0$, and collecting, for each coordinate $\boldsymbol{r}_0$, the resulting intensity

$$I(\boldsymbol{r}_0, \boldsymbol{r}) = \left| \left[\mathcal{L}_{\boldsymbol{r}_0}(\boldsymbol{r}) \mathcal{A}(\boldsymbol{r}) \right] * \mathcal{P}(\boldsymbol{r}) \right|^2 \tag{9}$$

where $\mathcal{A}$ and $\mathcal{P}$ are the same object transmittance and coherent PSF as in Equation (1), and $\mathcal{L}_{\boldsymbol{r}_0}$ is the Green's function propagating the field from the point-like source centered in $\boldsymbol{r}_0$ to the sample plane. As we shall discuss shortly, the wide freedom in the choice of $\mathcal{L}_{\boldsymbol{r}_0}$ (i.e., the illumination scheme) enables to greatly customize the optical performances of the 3D imaging system. Specifically, in order to encode 3D (light-field) information into $I(\boldsymbol{r}_0, \boldsymbol{r})$, illuminating the sample from many different "angles" is not necessary. In previous works (see, e.g., Ref. [19]), in fact, $\mathcal{L}_{\boldsymbol{r}_0}$ has always been arranged in such a way to have an illumination distance L between a source at coordinate $\boldsymbol{r}_0$ and the sample, such that the latter can be considered to be illuminated by tilted plane waves, corresponding to the choice

$$\mathcal{L}_{\boldsymbol{r}_0}(\boldsymbol{r}) = \exp\left[i \frac{2\pi}{\lambda} \frac{\boldsymbol{r}_0}{L} \cdot \boldsymbol{r} \right] \tag{10}$$

as conventionally done in tomographic systems. However, our complete formal analysis, and the consequent understanding of coherent imaging, enable to demonstrate that neither the angular illumination nor the requirement of collimated light are in any way necessary to encode 3D information into $I(\boldsymbol{r}_0, \boldsymbol{r})$. Most importantly, understanding the underlying physics of coherent and incoherent imaging is the key for achieving scanning-free direct 3D imaging, with no need for time-consuming phase retrieval algorithms.

The intensity distribution described by Equation (9) is easily recognized as a coherent image, as in Equation (1), with the object transmittance now replaced by the expression $\mathcal{L}_{\boldsymbol{r}_0} \mathcal{A}$, emphasizing the role of the illumination scheme and the wide freedom in its design. The acquired 4D intensity can thus be expected to have mostly the features we have attributed to coherent images, such as the decoupling of the lateral resolution and DOF. However, the large DOF entails the lack of axial localization: thick 3D samples are imaged with high transverse resolution, but lack any axial localization. To address the issue, we shall integrate the proposed technique with the properties of incoherent imaging, in which the tomographic properties are defined by the angular acceptance of the lens.

Fine isolation of a single axial plane of the sample can, in fact, be obtained through a Radon transformation of $I(\boldsymbol{r}_0, \boldsymbol{r})$, here expressed in a line integral formalism:

$$R_z(\boldsymbol{r}') = \int_{\gamma(\boldsymbol{r}')} I(\boldsymbol{r}_0, \boldsymbol{r})\, dl \tag{11}$$

which enables localizing the object within the much larger DOF characterizing coherent imaging (further details reported in the Supplemental Document). In Equation (11), $\gamma(\boldsymbol{r}')$ are two lines of equations $\sin\theta(z)\boldsymbol{r}_0 + \cos\theta(x)\boldsymbol{r} = \boldsymbol{r}'$ defined in the spaces (x_0, x) and (y_0, y). The Radon transform $R_z(\boldsymbol{r}')$ isolates a specific axial coordinate z by integrating over the whole dataset $I(x_0, x)$ at a z-dependent angle $\theta(z)$; this allows one to perform, in post-processing, a software z-scanning similar to the hardware scan done by manually moving the focus of a conventional (incoherent imaging) device. As detailed in the Supporting Information, the relation between the integration angle and the reconstructed axial plane can be understood in terms of how object points are mapped onto the detector, as a function of the illumination coordinate. The geometrical locus of the points of the sensor $\boldsymbol{r}$ corresponding to the same object coordinate $\boldsymbol{r}'$ is a line in the (x_0, x) space, with equation

$$\gamma(x') : \alpha(\delta)\, x_0 + \beta(\delta)\, x + x' = 0 \tag{12}$$

where α and β are two functions depending on both the defocusing distance δ and the particular illumination scheme, as is the case for conventional LF imaging. The same holds, with the same coefficients α and β, for the other two coordinates (y_0, y). Therefore, for an object placed at an axial displacement δ from the focused plane, the most accurate reconstructed image is $R_{z=\delta}$, as obtained by performing the integration in Equation (11) along lines at an angle $\theta = \arctan(-\alpha/\beta)$.

The analytical form of the Radon transform isolating the object plane $R_\delta = R_{z=\delta}$ has a particularly interesting form, namely

$$R_\delta(\boldsymbol{r}) = \left| \mathcal{A}(\boldsymbol{r}) * \tilde{\mathcal{P}}(\boldsymbol{r}) \right|^2 \tag{13}$$

with

$$\tilde{\mathcal{P}}(\boldsymbol{r}) = \mathcal{D}_{d(\delta)}(\boldsymbol{r}) * \mathcal{P}_0(\boldsymbol{r}) \tag{14}$$

where $\mathcal{P}_0$ is the "coherent" PSF of the imaging system in its focus, and $\mathcal{D}_\zeta$ is propagation in vacuum by a distance ζ, as in Equation (2). The properties of the reconstructed image are easily understood by noticing that Equation (13) is exactly the expression of a coherent image (see Equations (1) and (2)), as observed by the same imaging device, but affected by an "equivalent defocusing" $d(\delta)$. More specifically, reconstructed images are Rayleigh-limited at focus and show out-of-focus resolution scaling with $\sqrt{|d(\delta)|}$; the functional form of $d(\delta)$ depends on the

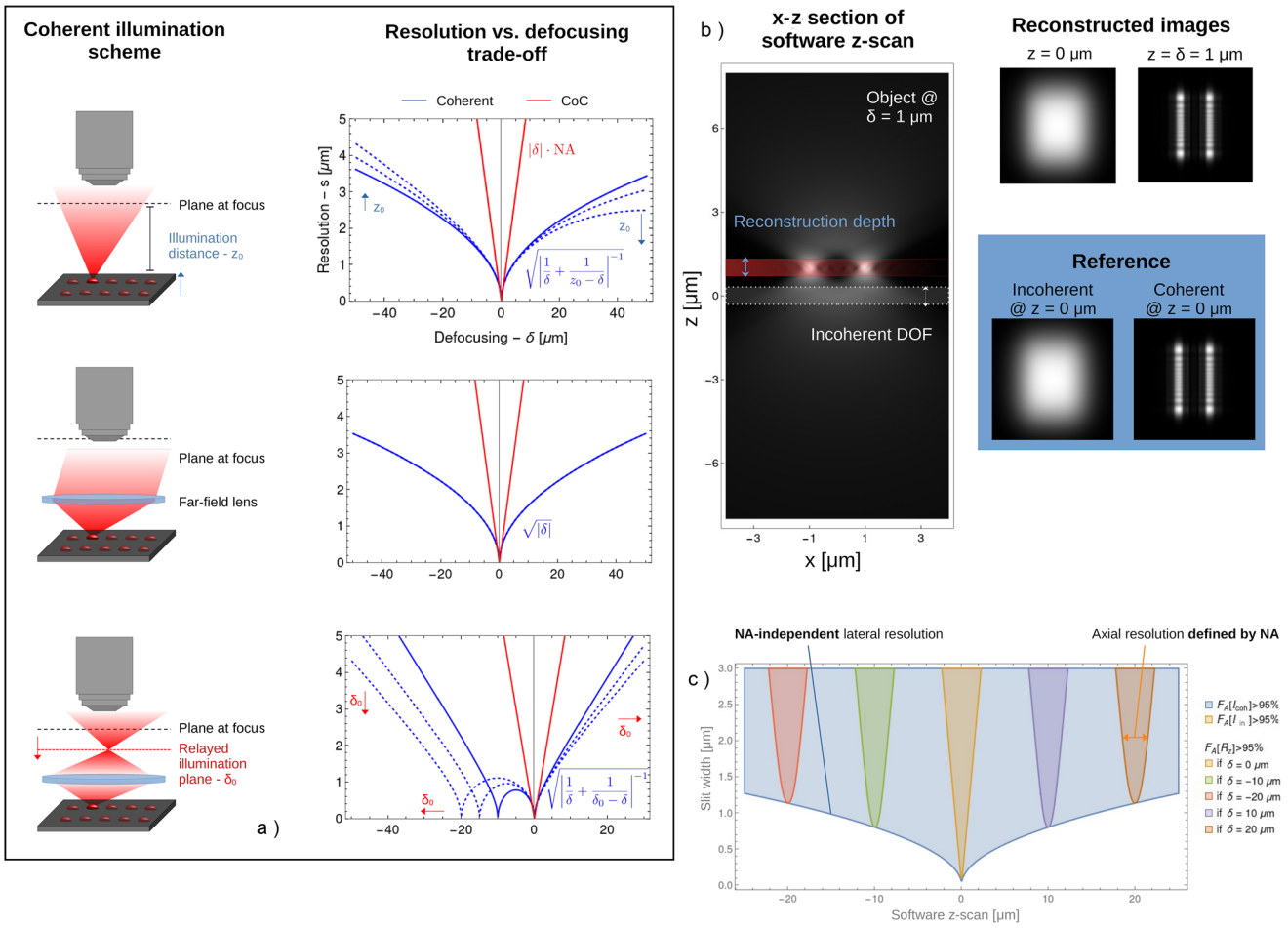

Figure 5. 3D imaging capability of a high-NA microscope exploiting spatial coherence. a) Three possible illumination schemes for performing 3D imaging through coherent illumination (left) and the corresponding scaling of the resolution as a function of defocusing δ (right). The plots compare the CoC-defined curve expected for incoherent illumination (red), with the square-root trends defined by coherence; different variations obtained within a given scheme by varying the illumination parameters (z_0 in the first case, δ_0 in the third case) are also reported (dashed blue lines). b) Axial section of a stack of reconstructed images $R_z(\boldsymbol{r})$ of a double slit mask placed at $\delta = 1\,\mu$m (left). On the top right, the two images reconstructed at focus $z = 0$ and at the correct sample locations $z = \delta = 1\,\mu$m are reported. As a reference, the two images of an unfocused incoherent and coherent system are reported from Figure 2. c) Characterization of the resolution as a function of the defocusing z for five different object positions δ, showing the sectioning capability and the overall resolution versus DOF performance of the proposed approach. The yellow and blue area are a reference for the performance of incoherent and coherent imaging, respectively; the last representing the maximum achievable DOF of the proposed technique. The five "V-"shaped areas show the sectioning capability enabled by the software z-scanning and the characterize the performance of the reconstructions, for the five different object placements; the software z-scan for a focused object (yellow) is shown to give the same resolution versus DOF performance as incoherent imaging.

illumination scheme adopted for illumination. As we shall see shortly, this implies that, for some illumination schemes, the optical performance of our technique can either match the performance of coherent imaging (if $d(\delta) = \delta - z$), or even be customized by designing the illumination stage to make such scaling more convenient for specific use cases. **Figure** 5a reports three possible illumination schemes, along with the expected resolution trend, as dictated by the functional dependence $d(\delta)$. For the upper illumination scheme, the illumination plane is placed at an arbitrary distance z_0 from the working distance of the microscope. In such system, the illumination function of Equation (9) is simply given by free-space propagation from the source plane to the sample, namely $\mathcal{L}_{r_0}(\boldsymbol{r}) = \mathcal{D}_{z_0-\delta}$. As detailed in the Supporting Information, the knowledge of $\mathcal{L}_{r_0}(\boldsymbol{r})$ allows one to easily calculate the coefficients α and β in Equation (12), and to perform the Radon transformation reconstructing the object plane. Such reconstruction has the form of Equation (13), with

$$d(\delta) = \left(\frac{1}{\delta} - \frac{1}{z_0 - \delta}\right)^{-1} \tag{15}$$

Illuminating the sample through simple free-space propagation is not the only scheme possible, as shown in the other two schemes reported in Figure 5a. Far-field illumination through a lens is also possible (middle panel), as well as near-field illumination through a lens relay system that transfers the image of the illumination stage in close proximity of the sample. The effect of different illumination stages is to modify $\mathcal{L}_{r_0}(\boldsymbol{r})$, and, in turn, to alter the functional form of the effective defocusing appearing in the Radon transforms. As the curves on the right part of the panel

indicate, the optical performance of the device can be modified to a large extent, offering a wide flexibility in view of a variety of different applications: the plots indicate that the scaling of the lateral resolution as a function of the defocusing is in a pure square-root relationship with defocusing only in the case of plane-wave illumination, namely, when $z_0 \to \infty$ in the first scheme, or when the middle scheme is adopted. This is a case in which the lateral resolution of the system perfectly matches a conventional coherent system. In the other situations, the lateral resolution is defined by the illumination parameters z_0 or δ_0.

Let us remark that the optical performance described by the curves in Figure 5a represents the lateral resolution retrieved by reconstructing the axial plane z corresponding exactly to the plane δ where the object is placed $R_\delta = R_{z=\delta}$ (Equation (13)). In real use cases, however, one typically does not have prior knowledge of the precise coordinate δ of the sample: to localize the sample on the axis, a stack of axial reconstructions R_z must be generated, for a set of axial coordinates z, and the correct reconstruction R_δ is recognized as the sharpest image of the "software" z-scan. This axial localization "a posteriori" is possible only because the resolution discussed so far is a property only of the image $R_{z=\delta}$, whereas all the other reconstructions $R_{z\neq\delta}$ retrieve a "blurred" image, as in incoherent imaging. This capability is what sets our system apart from a conventional coherent imaging device with fixed illumination, which lacks the possibility of axial localization.

The analogy with incoherent systems and the nature of "post-processing" blurring is most easily understood by considering the Radon transform retrieving the plane at focus. Such plane is recovered by summing all the coherent images together, regardless of illumination coordinate $\boldsymbol{r}_0$, without any transformation or, equivalently by integrating along the lines

$$\gamma_0(x') : x' = 0 \cdot x_0 - 1 \cdot x = x \tag{16}$$

Equation (11) thus becomes

$$R_0(\boldsymbol{r}) = \int I(\boldsymbol{r}_0, \boldsymbol{r})\, d\boldsymbol{r}_0 = I_{\text{inc}}(\boldsymbol{r}) \tag{17}$$

From an intuitive standpoint, in fact, integrating over the entire illumination plane is equivalent to shining uniform "incoherent" light onto the sample. This is the typically sought-after experimental condition of uniform illumination in conventional systems (e.g., Kohler illumination), here entirely achieved in post-processing. The mechanism responsible for blurring of the Radon transformations is thus the same responsible for background planes suppression (i.e., axial localization) in incoherent imaging.

The blurring caused by an imprecise reconstruction $R_{z\neq\delta}$ is shown in Figure 5b through simulations. The panel demonstrates that the great (NA-independent) DOF extension typical of coherent imaging is integrated with very accurate (NA-dependent) axial localization, due to the incoherent imaging properties brought in by the reconstruction process. The panel reports the (x, z) section of the 3D stack of reconstructed images $R_z(\boldsymbol{r})$ (left); the sample is a double slit mask placed at $\delta = 1\,\mu$m, showing accurate localization of the sample on the axis. The software z-scan demonstrates that the reconstruction process retrieves a sharp image of the sample only around the plane where the most accurate reconstruction happens. At a glance, the "depth" of the reconstruction is not what one would expect by coherent imaging, but rather similar to the native (NA-defined) incoherent DOF of the device. Qualitative similarities with the incoherent blurring and coherent images can also be recognized by considering the two images reconstructed at focus $R_{z=0}$, and at on the sample plane $R_{z=\delta}$, as reported in the top right panels; by comparison with the reference images within the blue outline, one immediately recognizes that the reconstruction at focus yields exactly the same blurred image as an incoherent system (left), whereas the sharpest reconstruction $R_{z=\delta}$ is identical to the corresponding coherent image (left). The reference images are, in fact, the same shown in Figure 1. The illumination scheme adopted for this simulations is the upper one of panel (a), with an illumination distance $z_0 = 110$mm.

To simultaneously demonstrate both the axial localization capabilities and the coherent lateral resolution, we assess the optical performance in terms of the image fidelity $F_A[R_z]$, as done in Figure 2. For the case of 3D imaging, the reconstruction requires the fidelity to be evaluated onto a three-parameter space: since the focus of the system is fixed at a given coordinate, both the relative position δ of the s-sized object and the reconstruction coordinate z can be moved independently with respect to the plane in focus. A quantitative description of the lateral and axial performance of the technique, referred to the same illumination scheme of panel (b), is reported in Figure 5c. As for Figure 2, the theoretical analysis performed on a Gaussian slit observed through the same Gaussian-apodized imaging system, is carried over in terms of the 95%-fidelity curves. To characterize the system, we have considered five axial placements of the sample along the optical axis $\delta = 0, \pm 10, \pm 20\,\mu$m; for each placement, the fidelity analysis has been performed on the whole stack of reconstructed images $R_z(\boldsymbol{r})$ and selected $F[I] = 95\%$ as a fidelity threshold. For reference, we have also reported the performance of incoherent (yellow) and coherent (blue) imaging in the (z, s) plane, with their characteristic linear (CoC-defined) and square-root trends. The five "V"-shaped areas, corresponding to the high-fidelity areas for the reconstructed stacks at the five different axial positions, show the simultaneous sectioning capability enabled by the software z-scanning and coherence-defined lateral resolution, and entirely characterize the optical performance of the technique for the five different object placements. Incidentally, the software z-scan for a focused object (yellow) cannot be distinguished by the performance of a conventional incoherent system. This confirms that our technique behaves as an incoherent imaging system in proximity of the focused plane, having the same Rayleigh-limited resolution and blurring dictated by the CoC. The CoC-defined linear scaling, however, also characterizes the "V"-shaped regions corresponding to the reconstructed stacks obtained from the four out-of-focus object placements (red, green, purple, and bronze regions). Reconstructions far from the plane in focus thus show the same "depth" as incoherent images, as defined by the incoherent suppression of background imposed by the NA. Nevertheless, the minimum detail size that can be faithfully reconstructed, as a function of the displacement δ, is defined by the resolution scaling of coherent imaging: as the plot shows, the boundary of the high-fidelity curve for coherent imaging corresponds precisely to the minimum resolution that can be resolved at a given

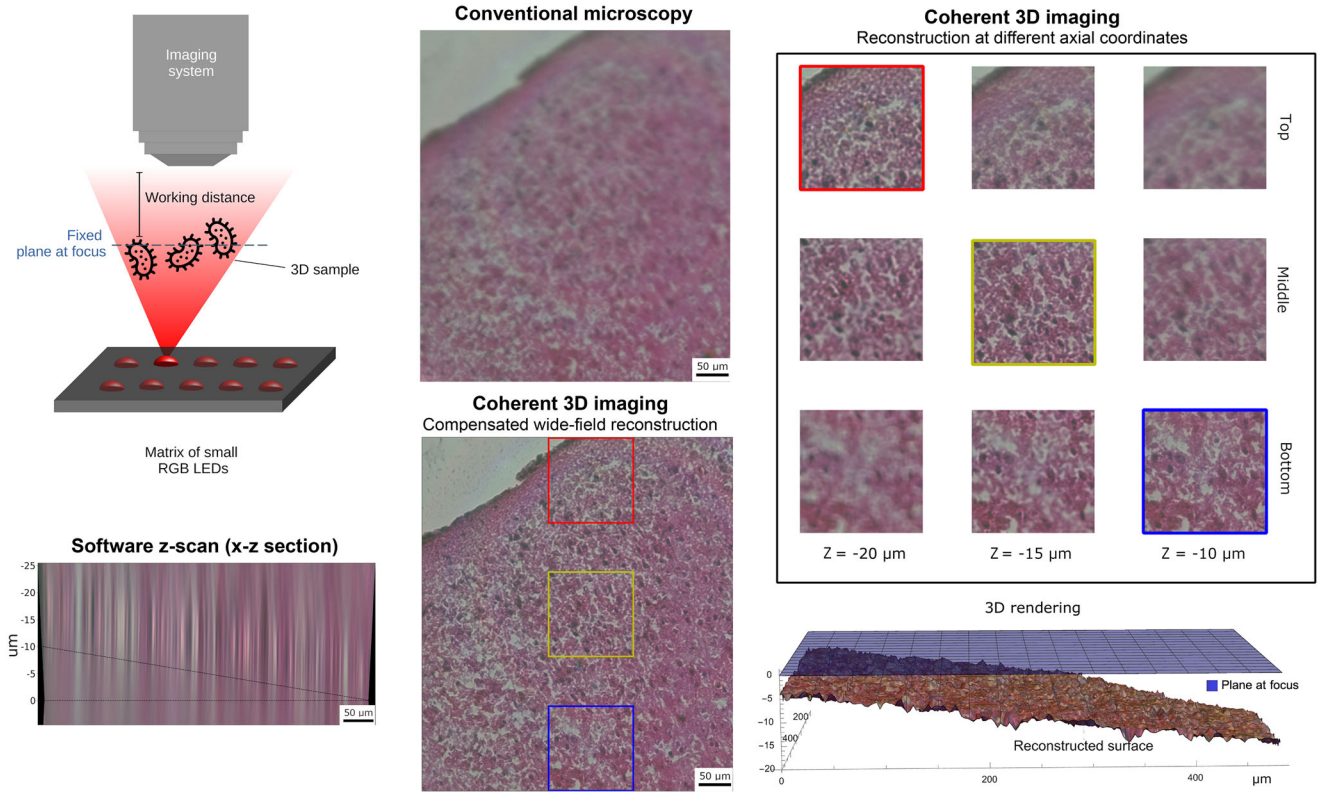

Figure 6. Multicolor 3D reconstruction of a histological mouse brain section exploiting spatially coherent illumination The resolution versus DOF advantage granted by spatially coherent illumination is used to reconstruct the true-color wide-field image a histological mouse brain section marked at two wavelengths. Due to both a slight tilting of the sample holder and a axial misplacement, conventional incoherent illumination yields an unfocused image. By exploiting sequential coherent illumination from an array of RGB LEDs, volumetric information is obtained and employed, through the software axial scans, for reconstructing the different portions of the sample at different z coordinates. The 3D information is then used to compensate for the tilting of about 10 degrees and obtain a single wide-field focused image. The optical microscope is a conventional 20×, 0.75 NA wide-field device.

displacement. In other terms, for each detail size, the DOF of the technique is defined by the coherent fidelity curve, as is the case for coherent imaging, but the axial resolution is defined by the much narrower, NA-dependent, incoherent CoC scaling.

3.2.2. Experimental Results

We shall now employ these results to experimentally demonstrate the high-resolution volumetric multicolor capability of the proposed technique (**Figure 6**). Coherent illumination from localized emitters is obtained through an array of commercial RGB LEDs placed far enough from the sample for the coherence area on the sample plane to be comparable with the details of interest. The sample is a 10 µm-thick mouse brain section, where cell nuclei and cytoplasm have been labeled, respectively, by hematoxylin and eosin. The acquired 3D information enabled us to compensate for the sub-optimal placement of the microscope slide, whose closest part to focus is 10 µm away from the focused plane; the sample was also mounted with a tilting of about 10 degrees, as shown by the 3D rendering, obtained by extracting the sharpest features from the 3D cube obtained via software z-scanning. Unlike the color-independent CoC, the square-root scaling of the resolution of coherent imaging has a weak dependence on wavelength ($\propto \sqrt{\lambda}$), thus giving rise to images characterized by negligible chromatic aberration.

A qualitative comparison with conventional microscopy and detailed information about data processing and image features can be found in the Supporting Information.

4. Discussion

As reported in Figure 1, the straight comparison between the z-scans of the volume surrounding a flat sample reveals evident differences when depending on the spatial coherence or incoherence of the illuminaton. The introduction of the image fidelity has enabled us to directly compare the performance of coherent and incoherent systems and to discover that, in coherent imaging, the degradation of the image resolution with defocusing is not related with geometrical blurring mechanisms such as the CoC. On the contrary, the degradation of the image quality is governed almost entirely by diffraction from the object plane to the imaged plane. This property has the formidable characteristic of being totally independent of the design of the imaging scheme, namely, on the size of the apertures involved and of the complexity of the system. The coherence-induced optical performance leads to a square-root law scaling of the resolution with

defocusing of the sample, as opposed to the linear scaling characterizing the CoC, as we derive from theory (Figure 2) and demonstrate experimentally (Figure 3). Interestingly, we found that the newly discovered square-root scaling, which could arguably depend on the particular test object on which the fidelity analysis is carried over, is common to a large class of object. As Figures 2-3 show, the trend is recovered, both experimentally and theoretically, on two very different classes of object and, as we report in the Supporting Information, also in the analytical case of a double-slit Gaussian sample. To the best of our knowledge, a different choice of the test objects only reflects on the value of a multiplying constant ($f_{\mathrm{diff}}(c)$ in Equation (8)), but does not affect the more physically interesting scaling $\sqrt{\lambda|z|}$.

Another interesting result is the fact that the transition between a regime in which the optical performance is dictated by incoherent effects to the coherent behavior occurs abruptly, as soon as the coherence area on the sample becomes comparable with the detail size. Namely, as long as the coherence area is small, interference effect between different parts of the sample can be neglected and the object features blur when defocusing; conversely, when the coherence area is large enough, the optical quality of the image can be basically understood in terms of the diffraction pattern generated by the sample on the plane in focus. This picture has less intuitive implications: it demonstrates that the maximum DOF that direct imaging can achieve is ultimately limited, at least in the realms of classical optics, by the spatial coherence of the illumination on the sample; this is in contrast with the approximately infinite DOF one might incorrectly expect by considering the case of collimated illumination; although one can expect to improve the DOF of the system by reducing the illumination NA, such improvement only happens as long as the resulting coherence area does not become too large. As the coherence area grows, the DOF enhancement loses its dependence from NA and comes out to be defined by the NA-independent coherent effects, as demonstrated in Figure 3. The transition from a linear, NA-dependent, resolution scaling to a square-root law can thus only be explained in terms of spatial coherence.

The discovery of a lateral resolution completely decoupled from the numerical aperture of the imaging system is a strong foundation for the introduction of a scanning-free 3D imaging modality. The underlying idea is to simultaneously rely on the enhanced lateral resolution and DOF inherited by coherent illumination, as well as on the fine tomographic reconstruction enabled by high-NA imaging systems. This has been demonstrated through comprehensive theory and simulation in Figure 5. Despite being based on the same image reconstruction principle as LF imaging, the coherent resolution scaling is increasingly more convenient at larger defocusing, with the additional benefit of retaining Rayleigh-limited resolution at focus. In fact, compared to conventional LF devices, which achieve DOF extension at the expense of lateral resolution, the DOF of 3D imaging systems based on spatially coherent illumination scales quadratically with the desired resolution, thus always yielding an advantage over the linear scaling typical of LF.[36] Additionally, since a high NA has no effect on the resolution and DOF of the system, large apertures can be used to obtain optimal sectioning capability upon refocusing, enabling a strong suppression of the background neighboring planes, as in high-NA tomographic systems.

The only factor potentially limiting the device performance might be the image degradation caused, in very thick and structured samples, by the coherent superposition of light from different axial planes. Samples of this kind are, however, knowingly difficult to image even in conventional wide-field absorption microscopy relying on z-scanning, due to the image degradation determined by the thickness separating the plane in focus from the sample surface.

For the sake of comparing the performance of coherent imaging to incoherent imaging, which is insensitive to the phase content of the sample, we have limited our analysis to non-phase object. However, coherent imaging is knowingly sensitive to the "complex" transmittance of the sample, so that the 3D imaging technique we propose can potentially be used as a "direct" imaging alternative to optical diffraction tomography.[37]

We should again remark that our proposal only requires transverse spatial coherence, and is insensitive to "temporal" incoherence. This is particularly relevant in view of "in vivo" biological applications, where negligible radiation damage is required.

As a final observation, we like to emphasize the enormous computational advantage offered by the image reconstruction based on Radon transform, as opposed to computational techniques based on coherence.[19,24,26] In fact, Radon transform can be performed in real-time with current GPU architectures and FPGAs,[38] or through the use of holographic screens.[39] The proposed 3D wide-field imaging technique has the full potential for being used for direct and real-time imaging. Its extreme simplicity, flexibility, and low cost, also compared to LF imaging, has high potential in view of using 3D imaging in new scenarios, ranging from the study dynamical processes to low-budget applications, and public healthcare in developing countries.

Supporting Information

Supporting Information is available from the Wiley Online Library or from the author.

Acknowledgements

G.M., B.B., F.V.P., G.P.N., and M.D. acknowledge funding from Universitá degli Studi di Bari through the Horizon Europe Seeds program, project INTERGLIO (S081). M.D. and F.V.P. acknowledge support by PNRR MUR Project No. PE0000023-NQSTI (National Quantum Science and Technology Institute). G.M. acknowledges funding under project ADEQUADE: this project has received funding from the European Defence Fund (EDF) under grant agreement EDF-2021-DIS-RDIS-ADEQUADE. G.P.N. is supported by: 1) AstroDyn (FA9550-19-1-0370), AstroColl (FA9550-21-1-00352) and Stochastic Biophysical Interactions within Aquaporin-4 Assemblies (FA9550-20-1-0324) funded by AFOSR; 2) Marie Skłodowska-Curie Actions -ITN-2020 ASTROTECH (GA956325) funded by the European Commission; 3) NEXTGENERATIONEU (NGEU) funded by the Ministry of University and Research (MUR), National Recovery and Resilience Plan (NRRP), project MNESYS (PE0000006) – A Multiscale integrated approach to the study of the nervous system in health and disease (DD 1553, 11.10.2022); 4) NEXTGENERATIONEU (NGEU) funded by the Ministry of University and Research (MUR), National Recovery and Resilience Plan (NRRP), project CN00000041 - National Center for Gene Therapy and Drugs based on RNA Technology (DD n.1035, 17.06.2022). Funded by the European Union. Views and opinions expressed are however those of the author(s) only and do not necessarily reflect those of the European Union

or the European Commission. Neither the European Union nor the granting authority can be held responsible for them.

Conflict of Interest

The authors declare no conflict of interest.

Author Contributions

G.P.N. and M.D. contributed equally to this work. G.M. conceptualized the idea, developed theory and simulations, designed and built the experimental setup, developed the software, performed data analysis, and wrote the original draft. G.M. and B.B. performed the experiments. B.B. prepared the histological sample and contributed to write the biological part in the Supplemental document. F.V.P. supervised the theoretical work. G.P.N. supervised the biological part of the work. M.D. supervised the overall physical part of the work. M.D. and G.S. contributed to the organization and writing of the manuscript M.D. and G.P.N. were responsible for fundings. All authors read and edited the manuscript.

Data Availability Statement

The data that support the findings of this study are available from the corresponding author upon reasonable request.

Keywords

3D imaging, 3D microscopy, coherent imaging, volumetric imaging

Received: November 9, 2023
Revised: March 6, 2024
Published online:

[1] D. B. Murphy, M. W. Davidson, *Fundamentals of Light Microscopy*, John Wiley & Sons, Hoboken, NJ **2012**, pp. 1–19.
[2] R. Fischer, Y. Wu, P. Kanchanawong, H. Shroff, C. Waterman, *Trends Cell Biol.* **2011**, *21*, 682.
[3] A. J. Ropelewski, M. A. Rizzo, J. R. Swedlow, J. Huisken, P. Osten, N. Khanjani, K. Weiss, V. Bakalov, M. Engle, L. Gridley, M. Krzyzanowski, T. Madden, D. Maiese, M. Mandal, J. Waterfield, D. Williams, C. M. Hamilton, W. Huggins, *Sci. Data* **2022**, *9*, 449.
[4] E. Beaurepaire, A. C. Boccara, M. Lebec, L. Blanchot, H. Saint-Jalmes, *Opt. Lett.* **1998**, *23*, 244.
[5] N. Eladawi, M. Elmogy, M. Ghazal, A. H. Mahmoud, H. Mahmoud, M. T. Alhalabi, A. Aboelfetouh, A. Riad, R. Keynton, S. Schaal, A. El-Baz, in *Diabetes and Fundus OCT*, Computer-Assisted Diagnosis, (Eds.: A. S. El-Baz, J. S. Suri), Elsevier, Cham **2020**, pp. 191–221. https://www.sciencedirect.com/science/article/pii/B9780128174401000073.
[6] A. A. Moiseev, G. V. Gelikonov, D. A. Terpelov, P. A. Shilyagin, V. M. Gelikonov, *Laser Phys. Lett.* **2012**, *9*, 826.
[7] T. S. Ralston, D. L. Marks, P. S. Carney, S. A. Boppart, *Nat. Phys.* **2007**, *3*, 129.
[8] E. H. Adelson, J. Y. A. Wang, in *IEEE Transactions on Pattern Analysis and Machine Intelligence*, **1992**, vol. *14*, pp. 99–106, https://doi.org/10.1109/34.121783.
[9] R. Ng, M. Levoy, M. Br, G. Duval, M. Horowitz, P. Hanrahan, D. Design, in *Stanford University: Computer Science Technical Report CSTR*, vol. *2*, Stanford University, Stanford, CA **2005**.
[10] M. Levoy, R. Ng, A. Adams, M. Footer, M. Horowitz, in *ACM SIGGRAPH 2006 Papers*, SIGGRAPH '06, Association for Computing Machinery, New York, NY, USA **2006**, pp. 924–934.
[11] M. Levoy, R. Ng, A. Adams, M. Footer, M. Horowitz, *ACM Trans. Graph.* **2006**, *25*, 924.
[12] M. Broxton, L. Grosenick, S. Yang, N. Cohen, A. Andalman, K. Deisseroth, M. Levoy, *Opt. Express* **2013**, *21*, 25418.
[13] R. Prevedel, Y.-G. Yoon, M. Hoffmann, N. Pak, G. Wetzstein, S. Kato, T. Schrödel, R. Raskar, M. Zimmer, E. S. Boyden, A. Vaziri, *Nat. Methods* **2014**, *11*, 727.
[14] P. A. Stokseth, *J. Opt. Soc. Am.* **1969**, *59*, 1314.
[15] V. Boominathan, K. Mitra, A. Veeraraghavan, in *2014 IEEE International Conference on Computational Photography (ICCP)*, IEEE, Piscataway, NJ **2014**, pp. 1–10.
[16] S. V. Aert, D. V. Dyck, A. J. den Dekker, *Opt. Express* **2006**, *14*, 3830.
[17] J. W. Goodman, *Introduction to Fourier Optics*, 3rd ed., Roberts & Co. Publishers, Englewood, CO **2005**.
[18] L. Tian, J. Wang, L. Waller, *Opt. Lett.* **2014**, *39*, 1326.
[19] L. Tian, L. Waller, *Optica* **2015**, *2*, 104.
[20] A. H. Fischer, K. A. Jacobson, J. Rose, R. Zeller, *CSH Protoc.* **2008**, *21*, https://doi.org/10.1101/pdb.prot4986.
[21] E. Hecht,*Optics*, Addison Wesley, San Francisco, CA **2002**, pp. 560–578.
[22] B. E. A. Saleh, M. C. Teich, Fundamentals of Photonics, John Wiley & Sons, Hoboken, NJ **1991**, pp. 342–383.
[23] D. Gabor, *Proc. R. Soc. A* **1949**, *197*, https://doi.org/10.1098/rspa.1949.0075.
[24] P. Ferraro, A. Wax, Z. Zalevsky, *Coherent Light Microscopy: Imaging and Quantitative Phase Analysis*, Springer, Berlin **2011**.
[25] J. Rodenburg, A. Maiden, *Ptychography*, Springer International Publishing, Berlin **2019**, pp. 819–904.
[26] G. Zheng, C. Shen, S. Jiang, P. Song, C. Yang, *Nat. Rev. Phys.* **2021**, *3*, 207.
[27] G. Zheng, C. Kolner, C. Yang, *Opt. Lett.* **2011**, *36*, 3987.
[28] Y. Zhang, Z. Cui, X. Ji, H. Wang, Q. Dai, *IEEE Access* **2019**, *7*, 129402.
[29] Y. Rivenson, Y. Zhang, H. Günaydın, D. Teng, A. Ozcan, *Light Sci. Appl.* **2028**, *7*, 17141.
[30] M. O. Scully, M. S. Zubairy, *Quantum Optics*, Cambridge University Press, Cambridge, MA **1997**.
[31] M. Mansuripur, *The van Cittert–Zernike theorem*, 2 edition, Cambridge University Press, Cambridge, MA **2009**, pp. 88–99.
[32] *Diffraction and Interference in Image Formation*, John Wiley & Sons, Hoboken, NJ **2012**, pp. 79–101.
[33] D. B. Murphy, M. W. Davidson, *Diffraction and Spatial Resolution*, John Wiley & Sons, Hoboken, NJ **2012**, pp. 103–113.
[34] G. D. Boreman, *Modulation Transfer Function in Optical and Electro-Optical Systems*, SPIE Press, New York **2001**.
[35] R. N. Bracewell, *Science* **1990**, *248*, 697.
[36] H. Zhu, M. Guo, H. Li, Q. Wang, A. Robles-Kelly, *IEEE Trans. Visualiz. Comput. Graph.* **2021**, *27*, 3019.
[37] O. Haeberlé, K. Belkebir, H. Giovaninni, A. Sentenac, *J. Mod. Opt.* **2010**, *57*, 686.
[38] G. Kertész, S. Szénási, Z. Vámossy, *2016 IEEE 20th Jubilee International Conference on Intelligent Engineering Systems (INES)*, IEEE, Piscatway, NJ **2016**, pp. 239–244.
[39] J. Wen, X. Yan, X. Jiang, Z. Yan, F. Fan, P. Li, Z. Chen, S. Chen, *Opt. Express* **2019**, *27*, 27441.